

*Iranian Journal of Oil & Gas Science and Technology*, Vol. 12 (2023), No. 2, pp. 13–39  
<http://ijogst.put.ac.ir>

## Integration of Seismic Attributes and Wellbore Data of Ghar Formation in the Hindijan and Bahregansar Oilfields

Mehrdad Safarpour<sup>1</sup>, Mohammad Ali Riahi <sup>2\*</sup>, Mehran Rahimi<sup>3</sup>

<sup>1</sup>M.S. Student, School of Mining Engineering, College of Engineering, University of Tehran, after Jalal Al Ahmad St., North Kargar St., Tehran, Iran.

<sup>2</sup>Professor, Institute of Geophysics, University of Tehran, Iran

<sup>3</sup>Ph.D. Candidate, Faculty of Earth Sciences, Shahid Chamran University of Ahvaz, Ahvaz, Iran

### Highlights

- An appropriate attributes selection process is a vital step in neural network implantation.
- Seismic attributes have shown a very good correlation with petrophysical parameters in the studied area.
- Using petrophysical information derived from seismic attributes, one can identify high hydrocarbon potential zones in the seismic section area.

*Received: April 5, 2022; revised: August 08, 2022; accepted: October 04, 2022*

### Abstract

The main purpose of this paper is to estimate and evaluate the petrophysical properties of the Ghar Formation in the Hindijan and Bahregansar oilfields using a combination of seismic and well logs data. In this study, following a step-by-step regression approach: first; sonic, density, and, porosity well-log data are collected. Second; seismic attributes, including amplitude, phase, frequency, and acoustic impedance are extracted from the seismic lines intersecting the wellbore locations. Then, using the MFLN and PNN intelligent systems, a relationship between porosity, shale volume, saturation, and seismic attributes is established. Using this relationship, the physical and petrophysical properties of the reservoir in the Ghar Formation are estimated and evaluated. We estimated the reservoir porosity between 15% and 20%, which is higher in the Hendijan oilfield as compared to the Bahregansar oilfield. The amount of water saturation in the Ghar formation varies between 25 and 30 percent. On the other hand, the amount of clay content and shale volume of the Ghar Formation in the Hendijan field is higher than that of the Bahregansar oil field.

**Keywords:** Bahregansar; Ghar formation; Hendijan; Neural networks; Seismic attributes.

### How to cite this article

Safarpour .M, Riahi. M.A, Rahimi.M., *Integration of Seismic Attributes and Wellbore Data of Ghar Formation in The Hindijan and Bahregansar Oilfields, Iran J. Oil Gas Sci. Technol.*, Vol. 12, No. 2, p.13-39, 2022.  
DOI: [10.22050/ijogst.2022.336225.1634](https://doi.org/10.22050/ijogst.2022.336225.1634)

## 1. Introduction

The Middle East hosts the world's thickest oil and gas reserves, most of which are placed on the Arabian Plate (Sharland et al. 2001). The thick accumulation of Cretaceous-age sediments in the Arabian Plate

\* Corresponding author:

Email: [mariahi@ut.ac.ir](mailto:mariahi@ut.ac.ir)

and the Zagros basin contains extremely massive and important hydrocarbon reserves (Setudehnia 1978; Alsharhan and Nairn 1986; Ghobeishavi et al. 2009 2010; Hollis 2011; Laponi et al., 2011) Misharif reservoir of the Cretaceous (Early Cenomanian-Turonian) is one of the most important hydrocarbon reservoirs in the South Pars Oil Field. Identifying the reservoir properties of the reservoir rock is one of the important factors in petroleum reservoir studies. Reservoir mapping is one of the most important steps in the evaluation and development of oilfields (Rastegarnia and Khadkhodaie, 2013). Today, due to the limitations in determining reservoir characteristics from wells, the use of indirect methods like high-level seismic data has become increasingly important in the estimation and evaluation of reservoir characteristics and appears to be an important factor in reducing the risk of drilling new wells. Seismic markers are mathematical functions derived from seismic information extracted from seismic data in the time and frequency domain. This basic information includes time, amplitude, frequency, and absorption, and these basic properties make it possible to classify the markers. Recent studies show that time-derived markers contain structural information and domain-derived markers include stratigraphic and reservoir information. Frequency-derived markers contain information on the properties of the reservoir. Energy absorption is another indicator that can provide information on fluidity and permeability (Brown, 2001). The importance of seismic drifting is due to the use of various data such as seismic information and well log data and geological information combined to enhance the resolution and accuracy of the reservoir model. In this study, a combination of 2D seismic data, well-log interpretive information like sonic, Gamma-ray, neutron data, and interpretive geological information related to the Ghar Formation in the Iranian oilfields of Hendijan and Bahregansar in the South Pars (Figure 1), as a model-based seismic inversion assay, was performed.

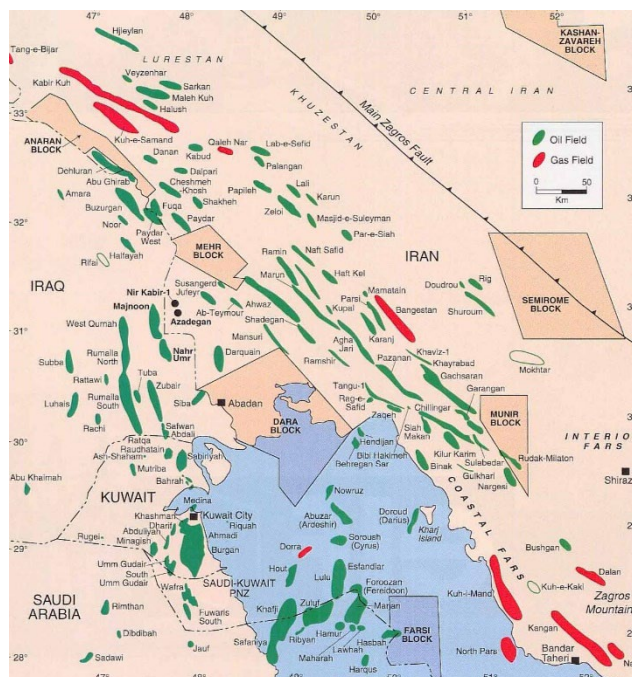


**Figure 1**

The location map of the Hendijan and Bahregansar oilfield (NIOC report).

The main purpose of seismic inversion in the studied oilfields is its national importance in modeling the South Pars basin. The strategic location of the South Pars and its oilfields has led to various studies and results. Many researchers including (Guning et al, 2007; Kadkhodaie-Ilkhchi et al., 2009; Yarmohamadi et al, 2014; Lang et al, 2017; Faraji et al, 2017; Maurya et al, 2017, 2018; Xu et al, 2019; Shiri and Falahat, 2019; Abdulaziz et al, 2019; Abdulaziz, 2020; Abdel-Fatah et al, 2020) used well

logs and seismic attributes to predict the petrophysical parameters of hydrocarbon reservoirs. In general, the workflow chart illustrates the steps involved in the present study displayed in Figure 2.

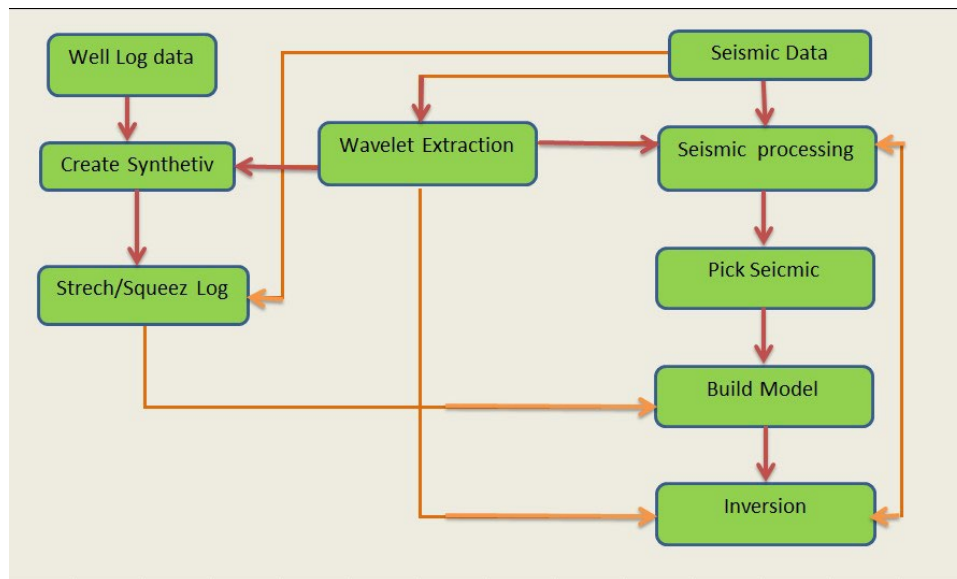


**Figure 2**

The workflow illustrates the steps involved in the seismic inversion process.

## 2. Geology of the area

The Hendijan and Bahregansar hydrocarbon fields are located northwest of the South Pars. Bahregansar Field is located 10 kilometers southeast of Hendijan Field and 56 kilometers from Bahregansar Oil Center. The geographical location of these fields is shown in Figure (2). The archipelago of Hindijan and Bahregansar fields contains eight independent tanks. Depending on the depth increase they are located in Ahvaz sandstone (gas Ghar), Ahvaz sandstone (oil Ghar) section of the Asmari a Formation, Asmari B, Sarvak, Kazhdomi (Naramer) gas, Fahliyan oilfield (Yamaha). Ten wells have been drilled in Bahregansar Field and five wells in Hendijan Field. The oil from the wells of Hendijan and Bahregansar Field was subdivided into two geographical units: sour oil (Hendijan field and Sarvak Behregansar field) and sweet oil (Ghar oil and Asmari Formation of Bahregansar field) and the resulting oil are transported to the Bahregansar oil Center onshore after mixing with a marine pipeline. Ahvaz sandstone section of the Asmari Formation in the Bahregansar and Hendijan oil field contains fine to medium-grained sandstones and Shaly thin strata (Figure 3). The source of this sandstone is from the west to the southwest of the South Pars. This sandstone extension in southwest Iran is seen as a fan and decreases from the source to the end of the sand. The average thickness of this section is about 89 meters in Bahregansar and Hendijan hydrocarbon fields. In the BS-10 well, the thickness of this sandstone is 94 meters, which is the maximum thickness of the sandstone in the field. (Geological Reports of Hendijan and Bahregansar Fields Offshore Oil Company).

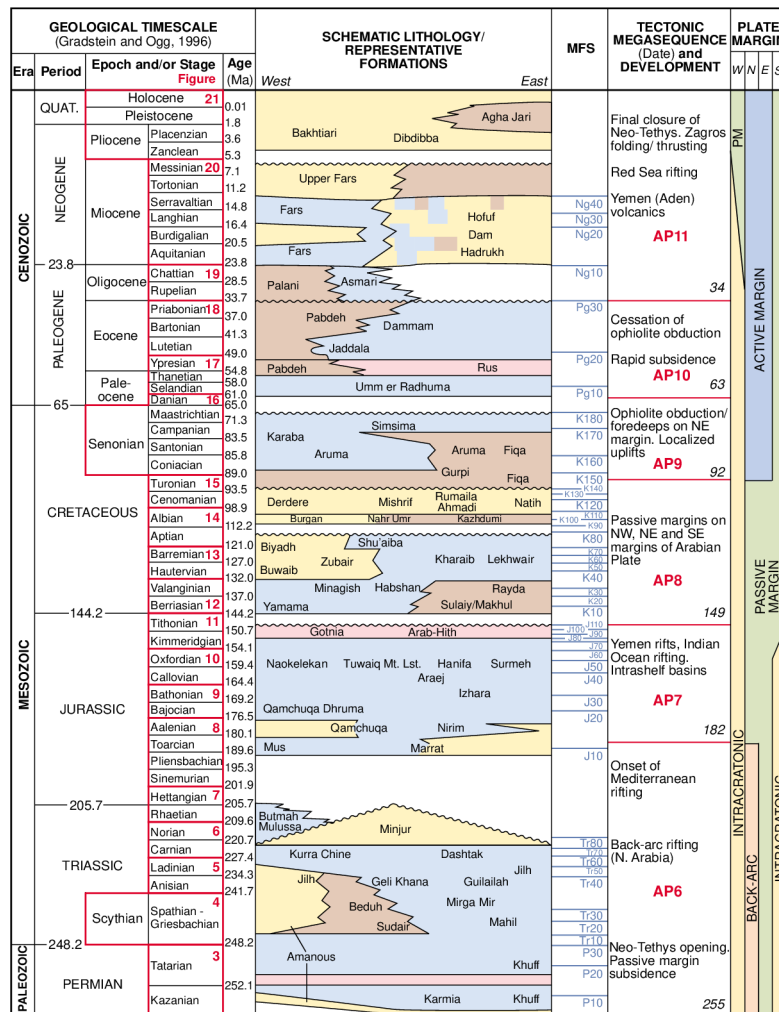


Figure 3

General stratigraphic column in the South Pars (Ziegler, 2001). The red numbers indicate Tectonostratigraphic Megasequences.

### 3. Methodology

In this study, petrophysical data along with seismic data were used to determine the reservoir parameters. Sonic, neutron, density, and gamma logs were used for petrophysics evaluation in the two different hydrocarbon reservoir fields. First, the time-depth relationship of sonic logs was corrected with the help of velocity information. Next, a synthetic seismogram was made with the help of a wavelet extracted from seismic information with a zero-phase wavelet. After comparison with adjacent vibration, a correlation was made between synthetic seismogram and real seismic data. The seismic data were then analyzed by the seismic inversion method (Russell 1988; Russell and Hampson 2006), which is described in detail below. In this research, rock physics studies have been used to reduce the effect of drilling fluids as well as wellbore wall collapse using petrophysical, sonic and density corrected logs. For this purpose, a hybrid model proposed by White (1991) was used, which is a numerical model based on the Custer and Toxose (1974) model. This model could establish the relationship between the elastic properties of rock structure, minerals, porosity, and percentage of clay (Sharifi et al, 2016; Sherif 2002).

## 4. Data description

### 4.1. Petrophysical evaluation

The petrophysical study of Bahregansar and Hendijan hydrocarbon fields was studied by collecting all the information of the existing well log and thoroughly examining them for two wells. In each hydrocarbon field, 4 to 6 wells are drilled at different locations. In most wells, the full set logs are not driven. Therefore, according to the need, the caliper log is used as a controlling tool for the wellbore diameter. After selecting the initial logs, the specified reservoir ranges from them, and petrophysical data were pre-processed. The results are finally obtained by combining well log data, core information, and production log information. Ahvaz sandstone (Ghar or Asmari sandstone) in this field consists of three layers separated by layers of shale. The upper two layers have very high porosity and contain condensate-rich intervals. The gas and water contact surface as shown in Figure 4 is about 2042 meters below sea level. The lower layer from 2042 meters contains petroleum and although it has good petrophysical properties from a reservoir point of view, it is of lower quality than the upper layers (Figures 4 and 5).

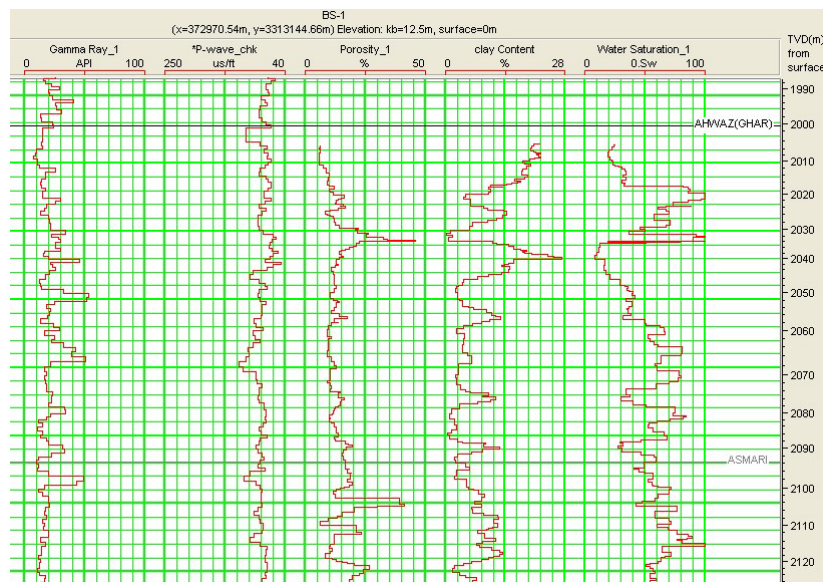


**Figure 4**

Interpreted results of Bahregansar Well #1 (shale volume, porosity, and water saturation).



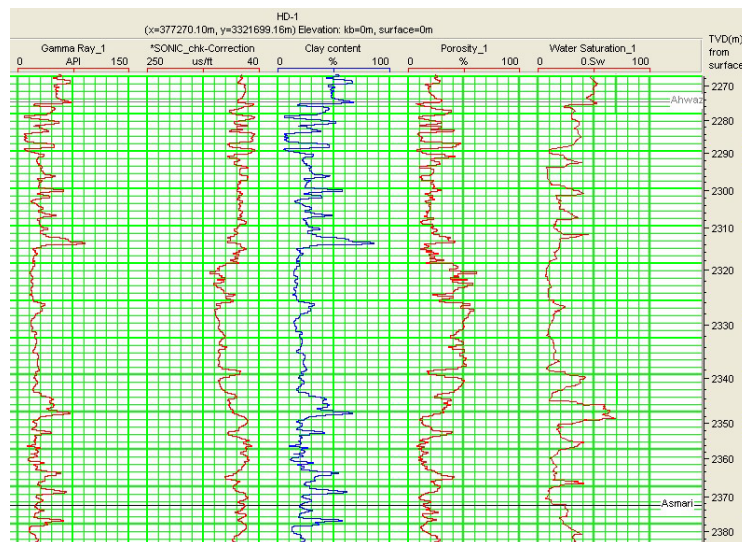


**Figure 5**

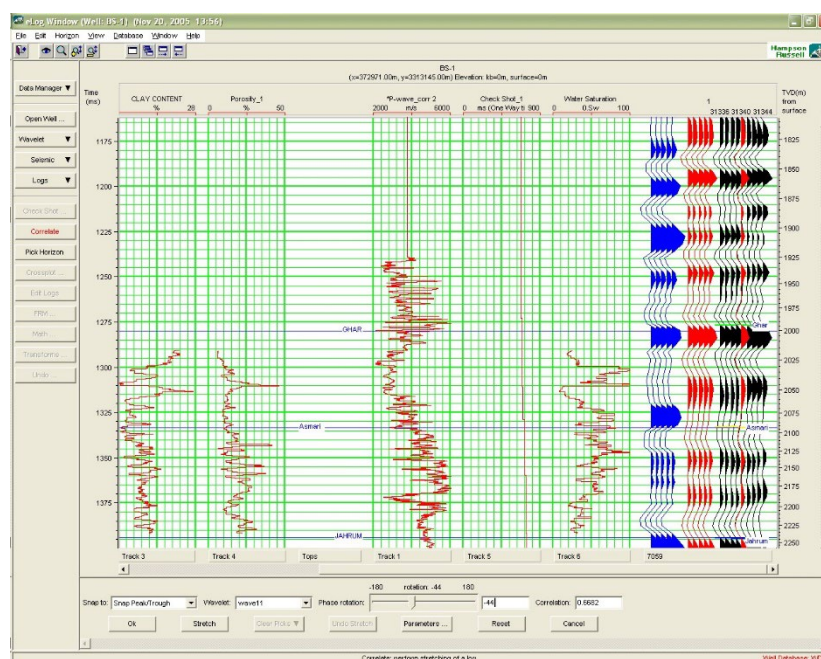
Well logs were obtained from the Hendijan well #1 (shale volume, porosity, and water saturation).

## 4.2. Seismic inversion

The purpose of seismic inversion is to estimate the acoustic impedance to better evaluate the reservoir for lithology, porosity, and reservoir fluid nature and to predict proper locations for subsequent drilling. Inversion is also one of the prerequisites for preparing information to predict and estimate important reservoir petrophysical properties, such as porosity and saturation.

### 4.2.1. Input information

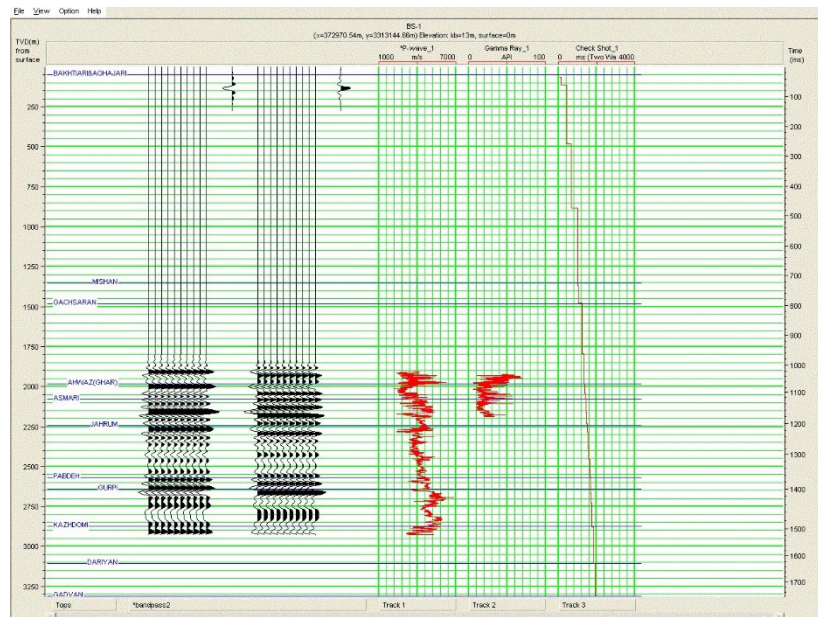
The data used as input in the seismic inversion algorithm included seismic line No. 7059 shown in Figure 6. Also, two wells were added in the inversion process as control points. These wells included sonic logs, drainage, effective saturation, effective porosity, gamma log, and shale volume. Interpreted horizons were introduced in the seismic stacked section through the inversion process. Thus, the initial information for inversion was efficient.



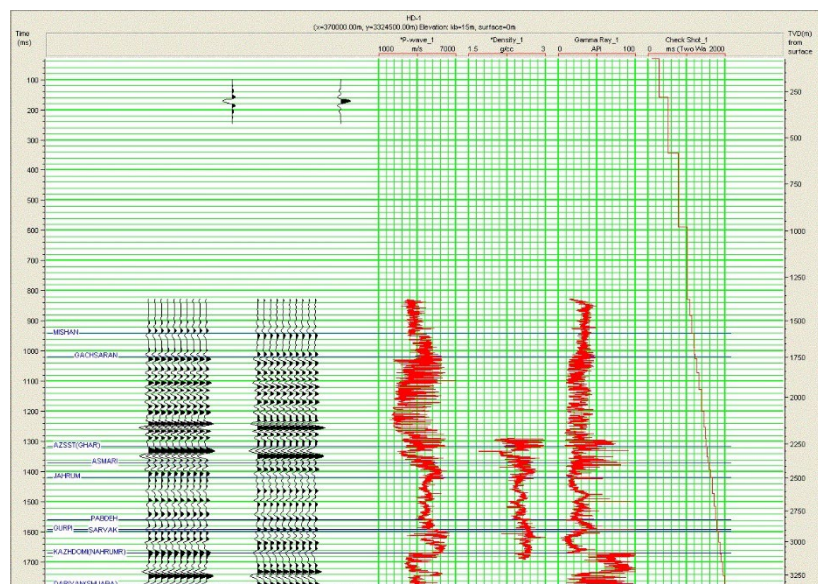
**Figure 6**

Correlation between real seismic data with well logs and synthetic seismogram for Bahregansar well #1.

The next step was to correct and correlate the well-logs with the check shots (Figures 7 and 8). As mentioned, prior to the preliminary interpretation, all wells had been analyzed to ensure that geological markers were correlated with the actual seismic reflectors. In this way, synthetic seismic was generated and correlated with a seismic section, to be used in the inversion process. Thus, the well-logs are transformed from the depth scale to the time scale and are overlaid on the seismic section.

**Figure 7**

Correlation between synthetic seismogram and check shot for the Bahergaran Wellbore #1.

**Figure 8**

Correlation between synthetic seismogram and check shot for the Handijan Wellbore #1.



#### 4.2.2. Wavelet extraction

After converting the well-logs scale from depth to time, it is time to extract a seismic wavelet using the match between the well-logs and the seismic section. Seismic wavelets can be extracted in three ways including statistical method, using the seismic stacked section, and well logs. As mentioned above, seismic operations were carried out in the field of the Hendijan hydrocarbon field using a gas gun source, so it can be expected that a similar wavelet to that produced by a gas gun could be obtained and the results obtained would be more reliable.

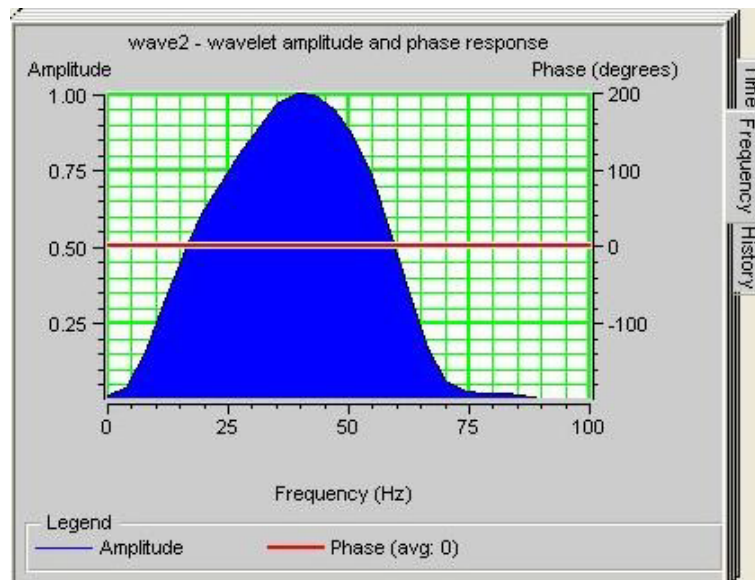


**Figure 9**

Shows a seismic wavelet that is statistically extracted from real seismic data.

Figure 10, shows a seismic wavelet that is statistically extracted from real seismic data. The center frequency of this wavelet is 35 Hz and its propagation length is 100 msec. This wavelet is a zero-phase wavelet.

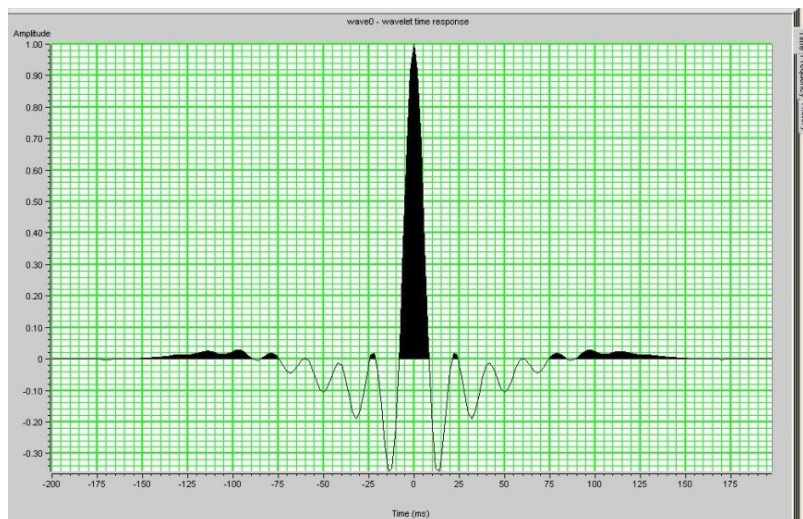


**Figure 10**

Statistical wavelet extracted from real seismic data in the time domain.



The second wavelet extracted based on real seismic data and well logs was used in the seismic inversion process. Figure 11 shows a wavelet extracted at the wellbore location using real seismic data and well logs. To obtain and extract this wavelet, a synthetic seismogram based on the sonic log and wavelet extracted from the real seismic was performed.

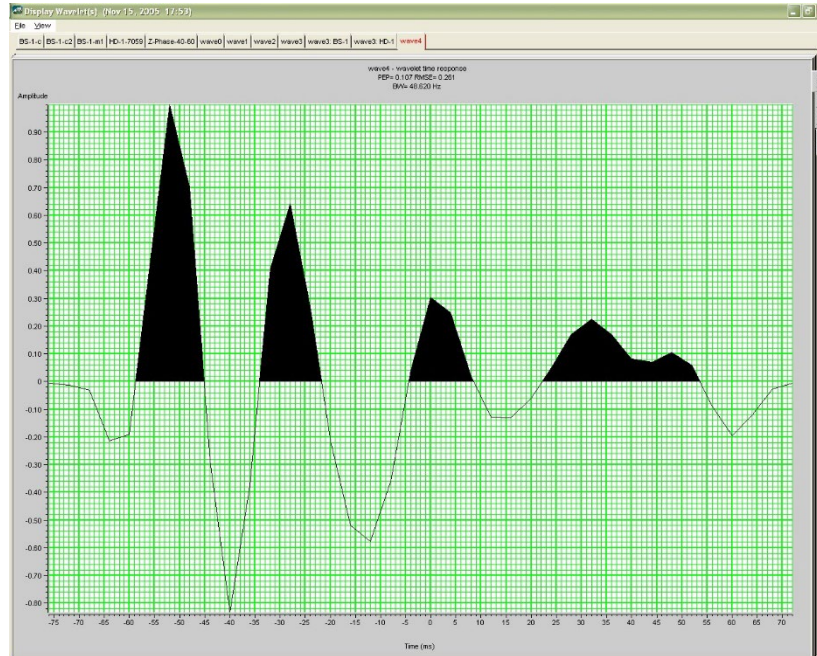


**Figure 11**

A seismic wavelet extracted from the well-log correlated with the seismic stacked section.

The final wavelet was a wavelet made from the combination of the first wavelet and the second wavelet. Figure 12 shows the wavelets obtained with respect to the method of the time and frequency domain.



**Figure 12**

Shows the wavelets obtained with respect to the method of the time and frequency domain.

Wavelet extraction, the phase of wavelet that was performed from seismic and well logs was shifted to -40 degrees and used as the final wavelet with a correlation coefficient of 70%. Then, the inversion process was performed.

#### 4.3. Seismic inversion process

Seismic data inversion on post-transposed data is a step in which we analyze the seismic section and attempt to construct an acoustic impedance model close to the actual ground model. The seismic inversion process is performed after we could construct the initial and homogeneous model. The methods selected for the seismic inversion algorithm were model-based and sparse spike methods. The model-based inversion was first introduced by Cook and Schneider (1983). The basis of this method is based on the behavior of the earth layer in the form of acoustic impedance blocks. In this method, first, an initial model of acoustic impedance contrast is prepared from well-logs (density and sonic logs) and then using Generalized Linear Inversion. Iteration in the inversion process was performed to minimize the difference between the initial model and the seismic section. The mathematical function for achieving the least desired difference (J) is as follows:

$$J = \text{Weight1} \times (T - W \times RC) + \text{Weight2} \times (M - H \times RC) \quad (1)$$

To achieve the final acoustic impedance the above relation was used. In the above relation, T is the synthetic seismogram, RC is the reflection coefficients, M is an estimation of the initial acoustic impedance model, W is wavelength amplitude and H is the degree of integration of the final reflection coefficients. This method is more sensitive to the original wavelet model than recursive methods (Geohorazone, 2002) and unlike sparse spike methods; information about reflection coefficients is not directly obtained from the seismic section therefore this method is not sensitive to the original wavelet model. One of the most important variable parameters in this method is the number of iterations of the acoustic impedance block (Russell, 1988; 2004). One of the disadvantages of the model-based inversion method is highly sensitive to the wavelet noise and its main advantages are its complete solution of the equation, the identification of errors during problem-solving, and the modeling of reflections.

In the sparse spike inversion method, events are calculated only where seismic information exists. This method produces the simplest model that contains information and details, and often low-frequency events are retrieved using geologic seismic information. This method is less dependent on the original model (Hampson, 2000).

In this method, the sequence of reflections is performed at one time as a spike, and the rest of the reflections are made step by step in the same order, and then the spiked are assembled in a time series and the model is designed. The seismic frequency domain is performed as follows:

$$x(w) = R(w)w(w) + N(w) \quad (2)$$

Here  $x(w)$  is synthetic seismogram,  $R(w)$  are reflection coefficient series,  $W(w)$  are seismic wavelets  $N(w)$  is noise, and  $w$  frequency. While a series of reflection coefficients are obtained, the acoustic impedance of each layer is calculated using the following relation:

$$z_{j-1} = Z_i \quad (3)$$

The solution seems to be to divide the synthetic seismogram's spectrum into the wavelet spectrum and obtain the resulting Fourier transform, including the disadvantages of the sparse spike method, which is to reduce the detail in the final output because only the block components in it are inverted. The

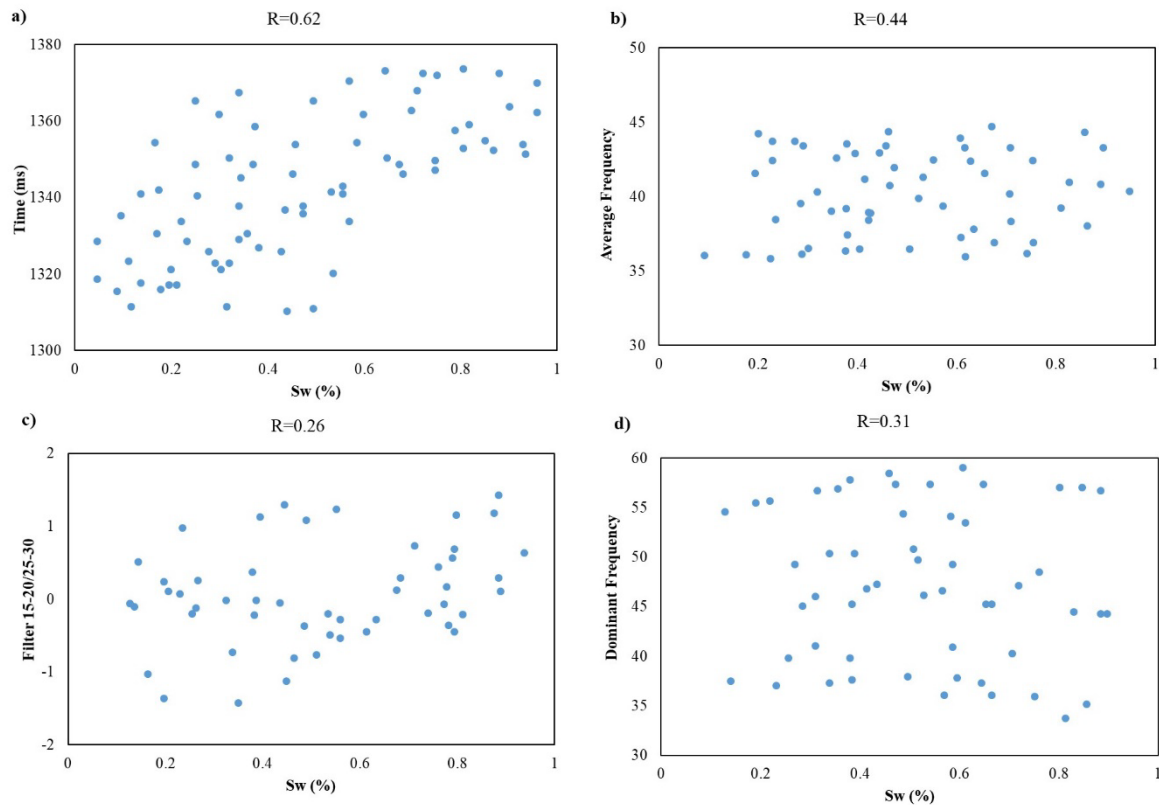
advantages of this method include the observational data in the calculations and the low-frequency information will be solved through its related equations. Finally, between these two methods, the sparse spike inversion method with a higher correlation coefficient of the selected data is used in the next step.

#### **4.4. Investigation of the results from multiple attributes and reservoir studies**

Standard seismic attributes were used as inputs to evaluate reservoir petrophysical properties including porosity, water saturation, and shale volume. Using a step-by-step regression approach, these input seismic attributes are combined and several composite attributes that are more sensitive to the reservoir properties are finally selected. To obtain each reservoir's petrophysical properties, these composite attributes were synthesized in the neural network algorithm. Table 1 shows the composition of different attributes and their correlation coefficients to the estimated porosity. Then, the correlation between the wellbore porosity and the estimated reservoir porosity was performed. Based on the results, we could select attributes that have a lower error percentage than the reservoir porosity. Then neural network system to obtain the desired petrophysical properties was performed, and finally, a cross-plot of the desired petrophysical properties along the seismic section is depicted.

##### **4.4.1. Seismic attributes selection**

Petrophysical properties prediction is achieved by integrating the interpreted petrophysical properties from obtained result analysis with both internal and external seismic attributes using a probabilistic neural network (PNN). The probabilistic neural network algorithm is a multilayered feedforward neural network derived from the integration of the Bayesian network with Fisher discriminant analysis. This algorithm is used in pattern recognition and dataset classification problems (Mohebbali et al., 2020; Mao et al., 2000; Berthold and Diamond, 1998). The manual and computer-aided PNN algorithms are evaluated over numerous trainings to determine the optimum number of attributes. This investigation uses seismic attributes to find the relation between the petrophysical properties and seismic attributes. In this section of this investigation, the relation between seismic attributes and petrophysical properties was investigated through the application of simple regression analyses (Kadkhodaie-Ilkhchi et al., 2009). Regression analysis is a practical method that is used to analyze the relationship between one dependent variable and several independent variables (Hampson et al., 2001; Mohebbali et al., 2020). A simple regression analysis was used to find the relationship between the seismic attributes and petrophysical properties. The obtained results from the regression analyses between the seismic attributes and petrophysical properties are shown in Figures 13 and 14. Figure 13 displays four cross plots between seismic attributes and water saturation with different correlation coefficients. Figure 14 displays seven cross plots between seismic attributes and porosity with different correlation coefficients. The amount of correlation coefficient values shown for each cross plot indicates the amount of the relationship between each seismic attribute with the related petrophysical properties.

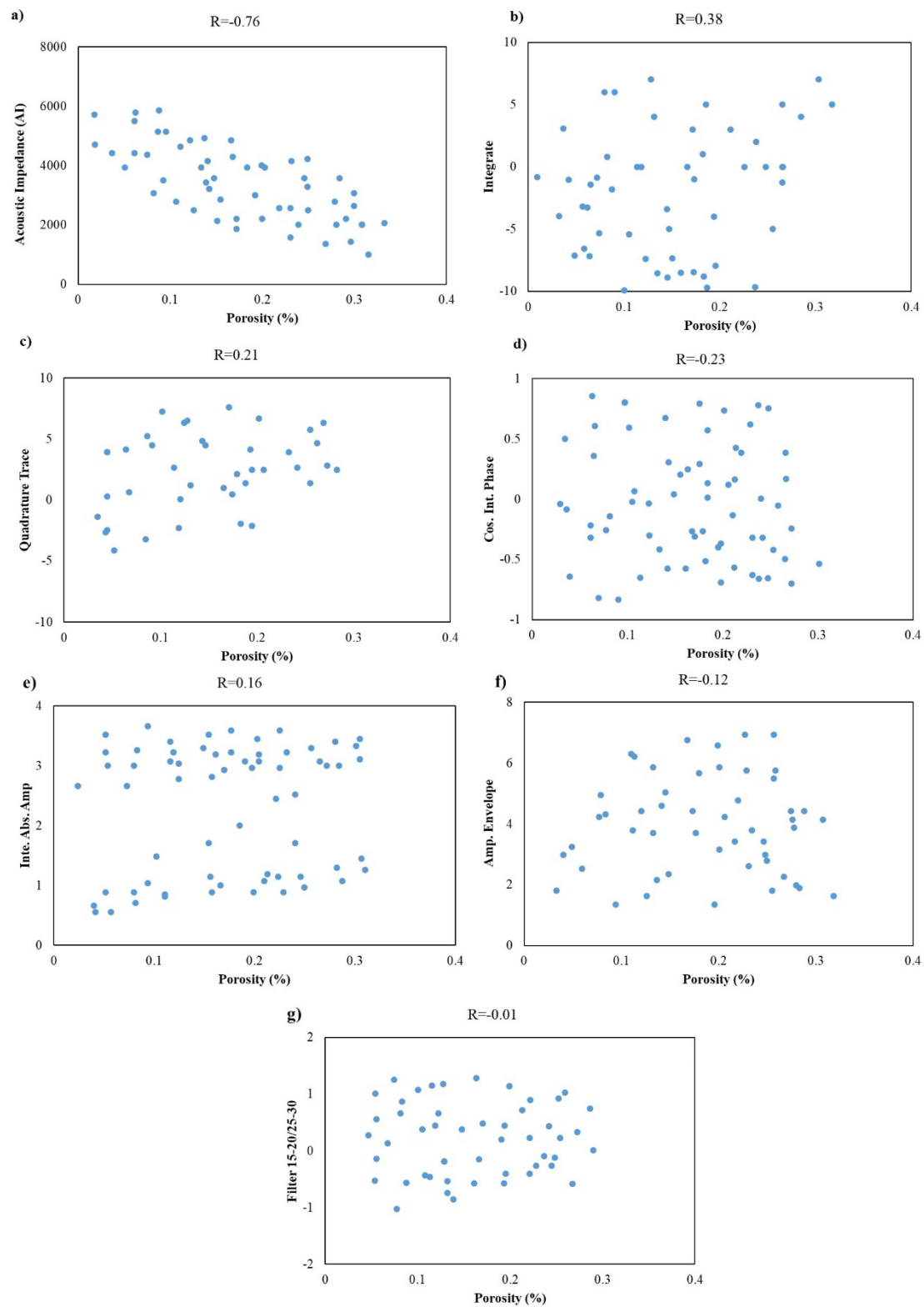


**Figure 13**

Cross-plots display relationships between seismic attributes and water saturation.

This study uses two approaches to data analysis. The first approach is water saturation analysis versus four seismic attributes, and the second approach is porosity analysis versus seven seismic attributes. The first approach is four attributes including time, average frequency, filter 15/20–25/30, and dominant frequency, and it can be considered for water saturation prediction. The relations between the water saturation and seismic attributes were shown in the cross-plot chart. Overall, the obtained result of seismic attribute analysis shows the different trends with water saturation including direct and reverse. The reservoir section due to the oil saturation decreases toward oil-water contact. Therefore, water saturation increases as depth increase across the hydrocarbon interval. The average frequency value is a signature of the geological feature and effects of the abnormal attenuation due to the effect of the hydrocarbon's media (Taner et al., 1994).



**Figure 14**

Cross-plots display relationships between seismic attributes and porosity.

The seismic filter 15/20–25/30 attribute is a dominant frequency filter and these attributes can be reflected in dominant frequency. As with the average frequency, the dominant frequency could be indicating abnormal frequency value attenuation. The obtained result of the seismic attribute analysis with porosity shows the different variations. Acoustic impedance value is a harvest of the velocity and density. The velocity and density have a good relation with porosity value and show the inverse relation. Integrate attribute is the sum of the amplitudes within the studied interval. Generally, this attribute is an indicator of an amplitude anomaly due to changes in the sedimentary facies. Quadrature trace attribute is evaluated from seismic trace analysis. Vertical variations of instantaneous phase reflect variations of the sedimentary facies. The instantaneous phase attribute is derived from the instantaneous phase. This attribute its fixed limitation value (1 to +1) is easier to understand, it can better identify variations in porosity and lithology. The amplitude envelope attribute is an indicator of the major sedimentary facies changes, and the same as the water saturation obtained, the dominate filter 15/20–25/30 can indicate porosity changes due to amplitude variations. Finally, the obtained result from the PNN algorithm with the best correlation at the evaluated wells is accepted as a petrophysical model capable of porosity and water saturation prediction of seismic data attributes.

#### **4.4.2. Porosity evaluation**

Standard seismic attributes were used as inputs to evaluate the porosity property. Using a step-by-step regression approach, these input attributes are combined and several composite attributes that are more sensitive to porosity properties are finally selected. To calculate the porosity of several composite attributes was performed in the previous step, then the neural network algorithm was implemented. Table 1 shows the combination of different attributes and their correlation coefficient of selected porosity properties. Table 2 shows the correlation between the well-log and the estimated porosity. Depending on the attitude of the selected attributes, the error value is reduced and the best combination of attributes is obtained in Table 2, for the ten bottom attributes.

**Table 1**

Composition of implemented attributes together with their correlation coefficient with the porosity parameter.

	<b>Attribute I</b>	<b>Attribute II</b>	<b>Correlation coefficient</b>
1	Raw seismic	Amplitude Weighted Cosine Phase	0.999935
2	Amplitude Envelop	Amplitude Weighted Frequency	0.98802
3	Average Frequency	Time	-0.98531
4	Average Frequency	dominate Frequency	0.984092
5	dominate Frequency	Time	-0.983376
6	Derivative	Quadrature Trace	-0.979774
7	Integrate	Quadrature Trace	0.968323
8	Amplitude Weighted Frequency	Integrated Absolute Amplitude	0.944861
9	Apparent Polarity	Time	0.938549
10	Raw seismic	Second Derivative	-0.936087
11	Amplitude Weighted Cosine Phase	Second Derivative	-0.935622
12	Amplitude Envelop	Integrated Absolute Amplitude	0.935109
13	Amplitude Weighted Frequency	Apparent Polarity	-0.908969
14	Amplitude Envelop	Apparent Polarity	-0.904966
15	Derivative	Integrate	-0.902692
16	Apparent Polarity	dominate Frequency	-0.897598
17	Average Frequency	Apparent Polarity	-0.893726
18	Amplitude Weighted Frequency	Time	-0.871787
19	Filter 35/40-45/50	Second Derivative	-0.86149
20	Amplitude Weighted Phase	Quadrature Trace	0.853539
21	Amplitude Weighted Phase	Integrate	0.848328
22	Amplitude Weighted Frequency	dominate Frequency	0.843297
23	Amplitude Weighted Cosine Phase	Cosine Instantaneous Phase	0.820266
24	Amplitude Envelop	Time	-0.819264
25	Raw seismic	Cosine Instantaneous Phase	0.818071
26	Amplitude Weighted Phase	Derivative	-0.81333
27	Amplitude Polarity	Integrated Absolute Amplitude	-0.812943
28	Integrated Absolute Amplitude	Time	-0.800868
29	dominate Frequency	Integrated Absolute Amplitude	0.792181

**Table 2**

Training error value of the used attributes related to porosity parameter.

	<b>Target</b>	<b>Final Attribute</b>	<b>Training error</b>
1	porosity	Derivative Instantaneous Amplitude	4.626667
2	porosity	Amplitude Polarity	4.067448
3	porosity	Time	3.484539
4	porosity	Filter 45/50-55/60	3.276893
5	porosity	Filter 55/60-65/70	3.128593
6	porosity	Second Derivative Instantaneous Amplitude	3.056415
7	porosity	Instantaneous phase	2.986613
8	porosity	Integrate	2.841265

9	porosity	Derivative	2.78919
10	porosity	instantaneous Frequency	2.701374
11	porosity	Second Derivative	2.626165
12	porosity	Amplitude Weighted phase	2.603198
13	porosity	Dominant Frequency	2.563996
14	porosity	Cosine Instantaneous Phase	2.3751
15	porosity	Filter 35/40-45/50	2.348985
16	porosity	Amplitude Weighted Frequency	2.341673
17	porosity	Filter 5/10-15/20	2.205167
18	porosity	Amplitude Weighted Cosine phase	2.159117
19	porosity	Integrated Absolute Amplitude	2.143518
20	porosity	Filter 15/20-25/30	2.123438
21	porosity	Average Frequency	2.117774
22	porosity	Filter 20/30-35/40	2.112364
23	porosity	Raw Seismic	2.1105
24	porosity	Quadrature Trace	2.109427
25	porosity	Amplitude Envelope	2.113276

After we obtained attributes that were more sensitive to the porosity parameter, we introduced these attributes into the neural network to estimate the porosity. In this study, due to the higher correlation coefficients of PNN and MFLN neural Networks, these two methods were used and finally selected they could produce the highest correlation value with the well-log's porosity (Figures 15 and 16).

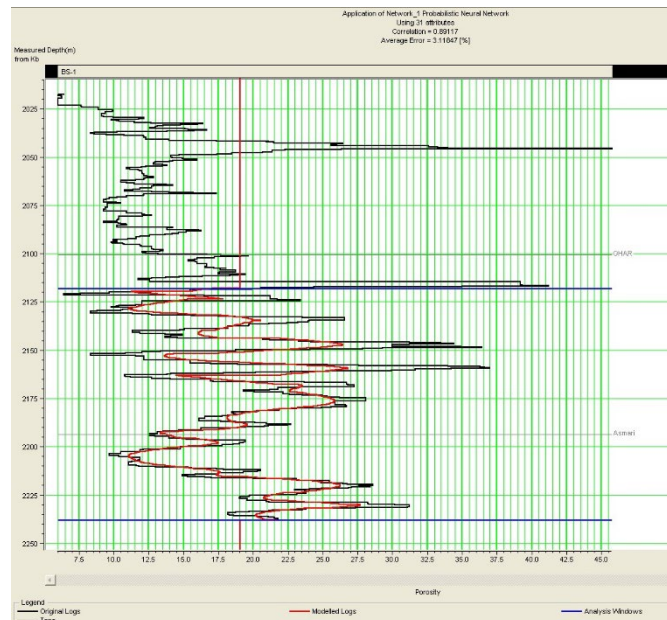


**Figure 15**

Correlation between the porosity obtained from well logs and the result obtained from the PNN network.

In the above figure, the measured porosity log from well logging is shown in black and the predicted porosity log obtained from the PNN is shown in red. The correlation coefficient between the porosity logs is 89%.



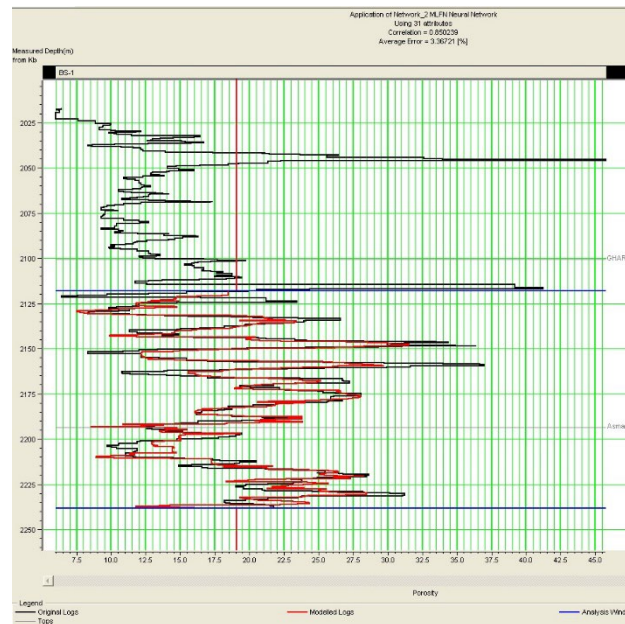


**Figure 16**

Correlation between the porosity obtained from well-logs and the result obtained from the MLFN network with an 85% correlation coefficient.

Based on training data in the neural network system, and its application to seismic data, porosity values across the seismic line were estimated throughout the region. Finally, by propagating the porosity results obtained from the PNN neural network and applying them to the seismic section, it produced the porosity distribution section across seismic line #7059 (Figure 17).

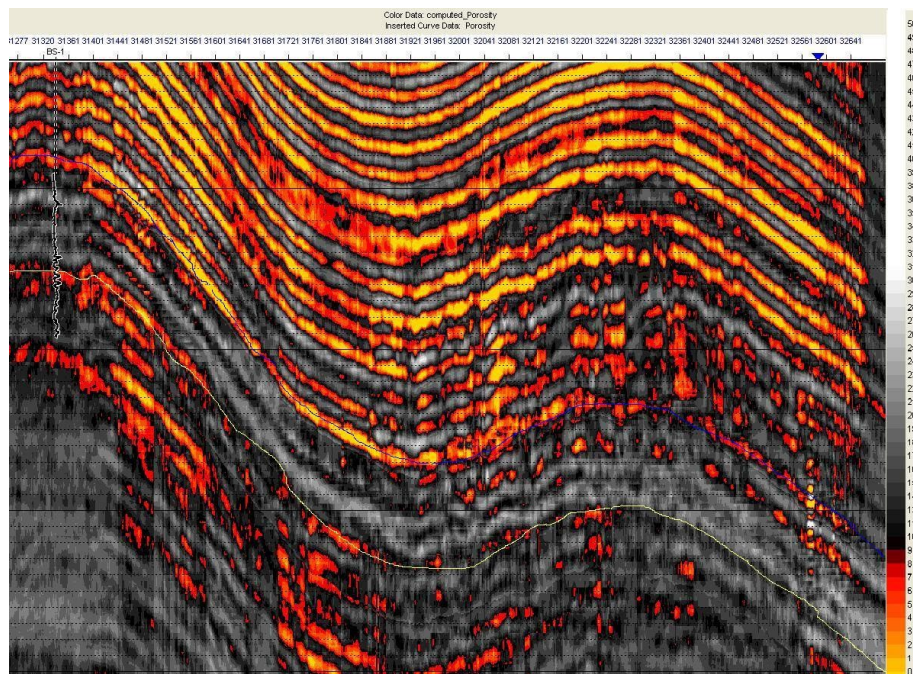


**Figure 17**

Overlaying porosity log obtained in the wellbore on the porosity section obtained across seismic line #7059 using neural network method.

As can be seen in Figure 17, the seismic horizons of the Ghar formation are divided into two separate units by the Shaly layer in both hydrocarbon fields. Namely, both reservoir is divided into two upper and lower parts of the Ghar Formation by a Shaly layer.

The amount of porosity obtained from seismic line #7059 is between 15% - 20%, which is higher in the Hendijan field than in the Bahregansar hydrocarbon field. It should be noted that the porosity values within the reservoir range (apex of the Ghar to apex of the Asmari horizon) are reliable at the well location. It should be mentioned that the calculations and extraction of the attributes are implemented within the working range of the repository.

#### 4.4.3. Saturation evaluation

Several standard seismic attributes were used as inputs to evaluate water saturation as presented in Table 3.

**Table 3**

Training error values of extracted attributes relative to water saturation.

	Target	Final Attribute	Training error
1	Sqrt (Water Saturation)	Filter 15/20-25/30	17.775746
2	Sqrt (Water Saturation)	Time	17.149495
3	Sqrt (Water Saturation)	Derivative	16.738882
4	Sqrt (Water Saturation)	Dominant Frequency	15.683496
5	Sqrt (Water Saturation)	Derivative Instantaneous Amplitude	14.824009
6	Sqrt (Water Saturation)	Filter 5/10-15/20	14.459009
7	Sqrt (Water Saturation)	Integrated Absolute Amplitude	13.631616
8	Sqrt (Water Saturation)	Amplitude Envelope	13.313927
9	Sqrt (Water Saturation)	Filter 25/30-35/40	12.780081
10	Sqrt (Water Saturation)	1/(Model Base)	12.643559
11	Sqrt (Water Saturation)	log(Band Limited)	12.509869
12	Sqrt (Water Saturation)	1/(LP-Spars Spike)	12.411149
13	Sqrt (Water Saturation)	Average Frequency	12.252408
14	Sqrt (Water Saturation)	Quadrature Trace	11.927377
15	Sqrt (Water Saturation)	Amplitude Weighted phase	11.813924
16	Sqrt (Water Saturation)	Second Derivative	11.67328
17	Sqrt (Water Saturation)	Raw Seismic	11.466588
18	Sqrt (Water Saturation)	Instantaneous phase	11.361309
19	Sqrt (Water Saturation)	Filter 55/60-65/70	11.297807
20	Sqrt (Water Saturation)	Colored	11.245899
21	Sqrt (Water Saturation)	Amplitude Weighted Cosine phase	11.21087
22	Sqrt (Water Saturation)	Cosine Instantaneous Phase	11.192933
23	Sqrt (Water Saturation)	Filter 45/50-55/60	11.154887
24	Sqrt (Water Saturation)	Filter 35/40-45/50	11.129155
25	Sqrt (Water Saturation)	Apparent Polarity	11.107884
26	Sqrt (Water Saturation)	Integrate	11.098634
27	Sqrt (Water Saturation)	Second Derivative Instantaneous phase	11.090051
28	Sqrt (Water Saturation)	Instantaneous Frequency	11.040899
29	Sqrt (Water Saturation)	Amplitude Weighted Frequency	11.040635
30	Sqrt (Water Saturation)	1/ (ML-Spars Spike)	11.069533

The stepwise regression algorithm was combined with these input attributes and 15 composite attributes were extracted, which are presented in Table 4.

**Table 4**

Composite attributes extracted to calculate water saturation.

1	Water Saturation	Log (Colored)
2	Water Saturation	Amplitude Weighted Frequency
3	Water Saturation	Instantaneous phase
4	Water Saturation	Filter 35/40-45/50
5	Water Saturation	Amplitude Envelope
6	Water Saturation	(Neural Network) <sup>2</sup>
7	Water Saturation	Apparent Polarity
8	Water Saturation	Filter 5/10-15/20
9	Water Saturation	Integrate
10	Water Saturation	Derivative
11	Water Saturation	Filter 25/30-35/40
12	Water Saturation	Amplitude Weighted Cosine phase
13	Water Saturation	Derivative Instantaneous Amplitude
14	Water Saturation	Raw Seismic
15	Water Saturation	Filter 45/50-55/60
16	Water Saturation	Time
17	Water Saturation	Cosine Instantaneous Phase
18	Water Saturation	Quadrature Trace

To calculate the water saturation of these 18 composite attributes performed in the previous step, the PNN neural network algorithm was applied. Figure 18 shows the water saturation correlation between the well-logs from the Bahregansar Well #1 and the estimated porosity from the seismic section.

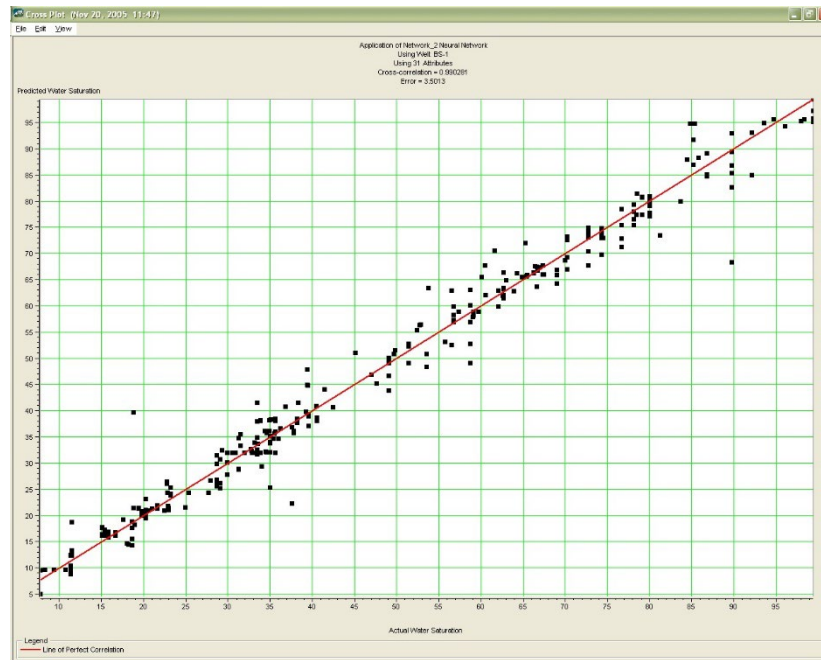


**Figure 18**

Cross-plot between the values of water saturation log from the wellbore and the neural network results at the Bahregansar Wellbore #1.

Based on training on the neural network and its application to seismic data, water saturation values across the seismic line were estimated throughout the reservoir region. Figure 19 shows the water saturation results obtained from the neural network.

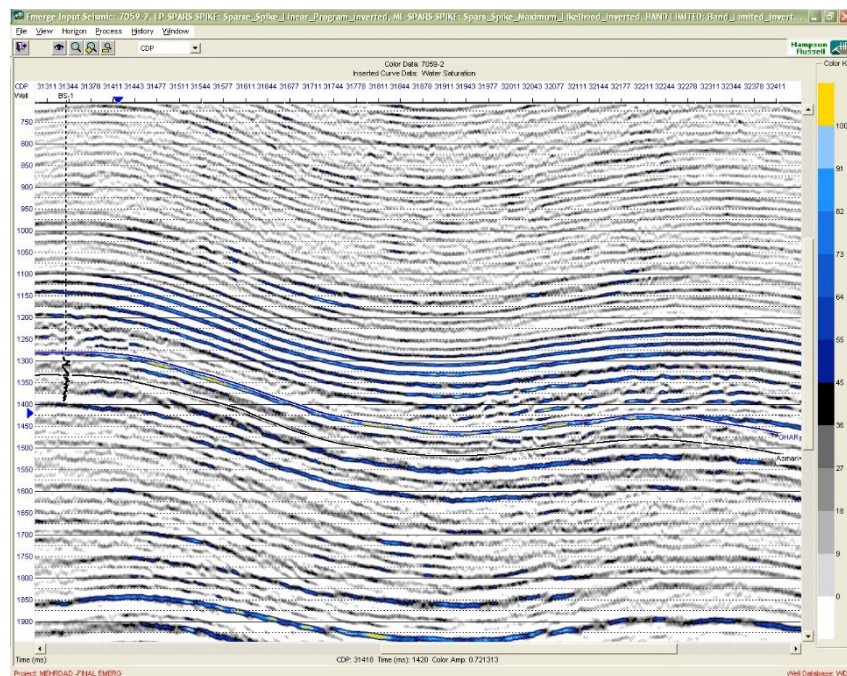


**Figure 19**

Overlaying the water saturation log (BS-1) on the estimated water saturation from the seismic section using a neural network for the Ghar formation across seismic line # 7059.



As can be seen in figure 19, the presence of a high-water saturation region indicates the presence of a separating shale layer. The amount of water saturation is lower in the upper part of the reservoir. The water saturation is obtained from 5% to 30% which is consistent with the well-log data in the wellbore location. This correlation is due to the full coverage of seismic data in the wellbore location.

#### 4.4.4. Evaluation of shale volume

The combination of available attributes was used to obtain the best correlation between them with respect to the shale volume parameter. Tables 5 and 6 show which attribute is most sensitive to shale volume.

**Table 5**

Combination coefficient of the different attributes in obtaining the best correlation between them with respect to the shale volume parameter.

	Attribute type 1	Attribute type 2	Correlation
1	Raw Seismic	Amplitude Weighted Cosine Phase	0.999942
2	Amplitude Envelop	Apparent Polarity	-0.999335
3	Derivative	Integrate	-0.999166
4	Amplitude Weighted Frequency	Integrated Absolute Amplitude	0.992784
5	Amplitude Envelop	Amplitude Weighted Frequency	0.987768
6	Amplitude Weighted Frequency	Apparent Polarity	-0.986246
7	Amplitude Envelop	Integrated Absolute Amplitude	0.983406
8	Apparent Polarity	Integrated Absolute Amplitude	-0.98183
9	Integrate	Quadrature Trace	0.97864
10	Derivative	Quadrature Trace	-0.9773
11	Raw Seismic	Second Derivative	-0.930626
12	Amplitude Weighted Cosine Phase	Second Derivative	-0.930219
13	LP-Spars Spike	Filter 5/10-15/20	0.898354
14	Filter 35/40-45/50	Second Derivative	-0.892154
15	Amplitude Weighted Frequency	Time	-0.877295
16	LP-Spars Spike	Band Limited	0.870646
17	Integrated Absolute Amplitude	Time	-0.868707
18	Amplitude Weighted Phase	Quadrature Trace	0.849809
19	Amplitude Envelop	Time	-0.823013
20	Amplitude Weighted Cosine Phase	Cosine Instantaneous Phase	0.821894
21	Amplitude Weighted Phase	Integrate	0.821698
22	Apparent Polarity	Time	0.820659
23	Raw Seismic	Cosine Instantaneous Phase	0.8199
24	Amplitude Weighted Phase	Derivative	-0.813668
25	ML-Spars Spike	Model Base	0.782669

**Table 6**

Shale volume correlation coefficient extracted from different attributes in the Hendijan and Bahergaran hydrocarbon fields.

Type	Attributes	Correlation
1	Derivative Instantaneous Amplitude	4.601699

2	1/ (Model Base)	4.017773
3	Filter 35/40-45/50	3.776103
4	Second Derivative	3.621082
5	(ML-Spars Spike) **2	3.471372
6	Filter 25/30-35/40	3.375977
7	Instantaneous Frequency	3.23231
8	Second Derivative Instantaneous Amplitude	3.167066
9	Quadrature Trace	2.9449
10	(Neural Network) **2	2.852324
11	Filter 25/30-35/40	2.79006
12	Instantaneous Frequency	2.696409
13	Instantaneous phase	2.634277
14	(Band Limited) **2	2.346846
15	Filter 45/50-55/60	2.321278
16	Dominant Frequency	2.312086
17	Amplitude Weighted Cosine phase	2.262963
18	Integrated Absolute Amplitude	2.252725
19	1/(Colored)	2.243289
20	Cosine Instantaneous Phase	2.229429
21	1/(LP-Spars Spike)	2.216842
22	Amplitude Weighted Frequency	2.207701
23	Raw Seismic	2.199784
24	Filter 15/20-25/30	2.192861
25	Apparent Polarity	2.188957
26	Filter 5/10-15/20	2.186027
27	Derivative	2.183813
28	Filter 55/60-65/70	2.182343
29	Average Frequency	2.182343
30	Integrated	2.182434
31	Amplitude Envelope	2.183126

Figures 20, and 21 show cross-plots of the results obtained from the MFLN neural network method and well log at Bahregansar Well #1, respectively.

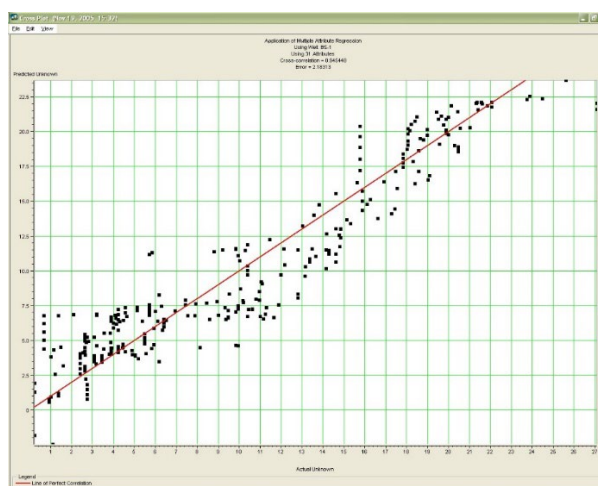


**Figure 20**

Relationship between actual shale volume from well logging at Bahregansar Well #1 location and predicted values using the MFLN neural network at the same wellbore with a correlation coefficient of 94%.

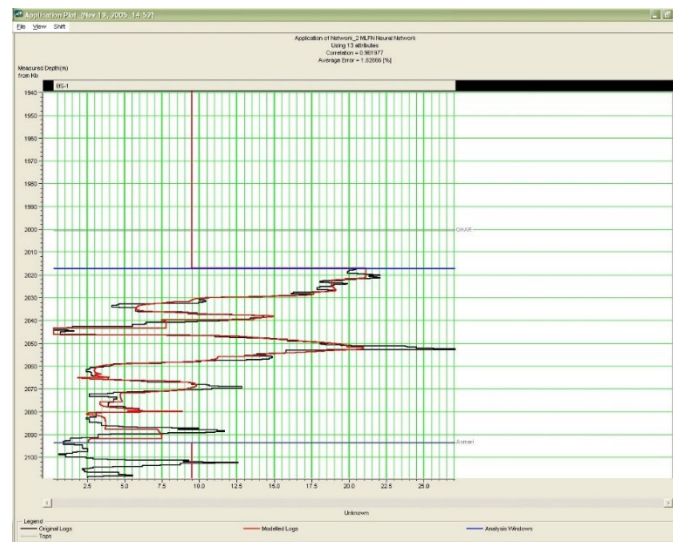


**Figure 21**

Comparison between shale volume obtained from the well-log and the MFLN neural network predicted results at the same wellbore with a correlation coefficient of 96%.

Figures 22, and 23 show cross-plots of the results obtained from the PNN neural network method and well log at Bahregansar Well #1, respectively.

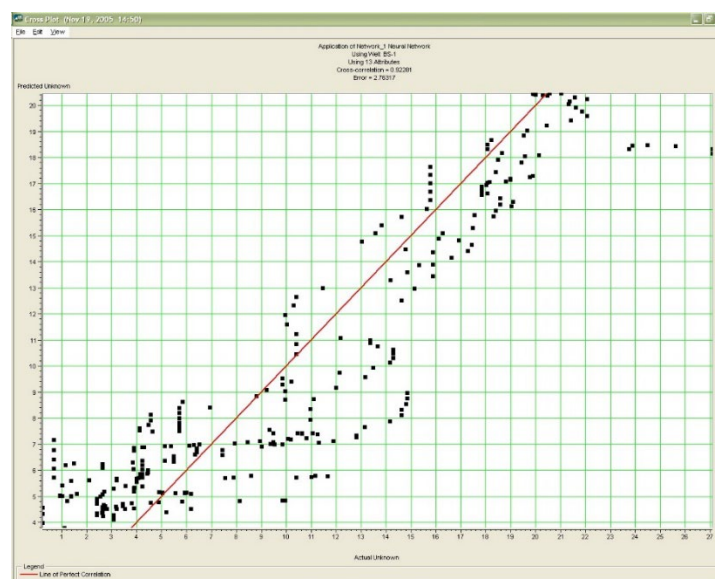


**Figure 22**

Relationship between the actual amounts of shale volume obtained from the well-log and the predicted value using the PNN neural network with a correlation coefficient of 92%.

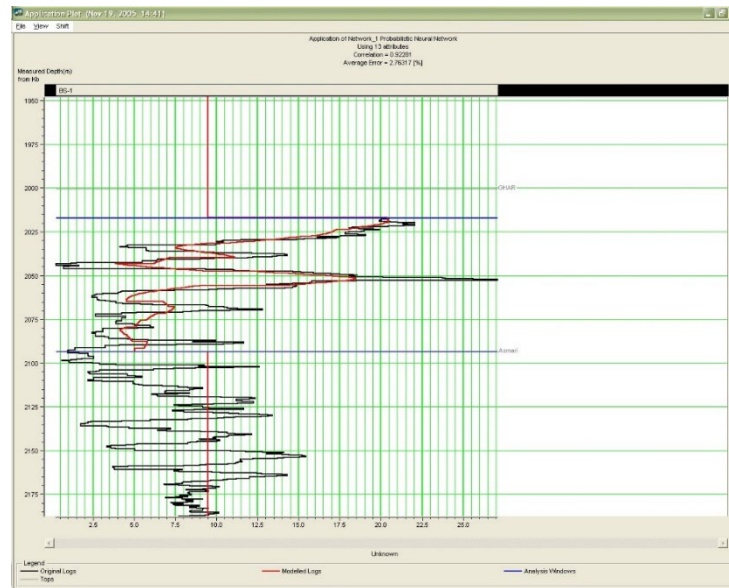


**Figure 23**

Shale volume log obtained from wellbore and shale volume log estimated from the PNN neural network at the Bahregansar well#1 with 92% correlation coefficient.

Based on training data in the neural network system, and its application to seismic data, shale volume across the seismic line was estimated throughout the region. Finally, by propagating the shale volume results obtained from the PNN neural network and applying them to the seismic section, it produced the shale volume distribution section across seismic line #7059 (Figure 24).

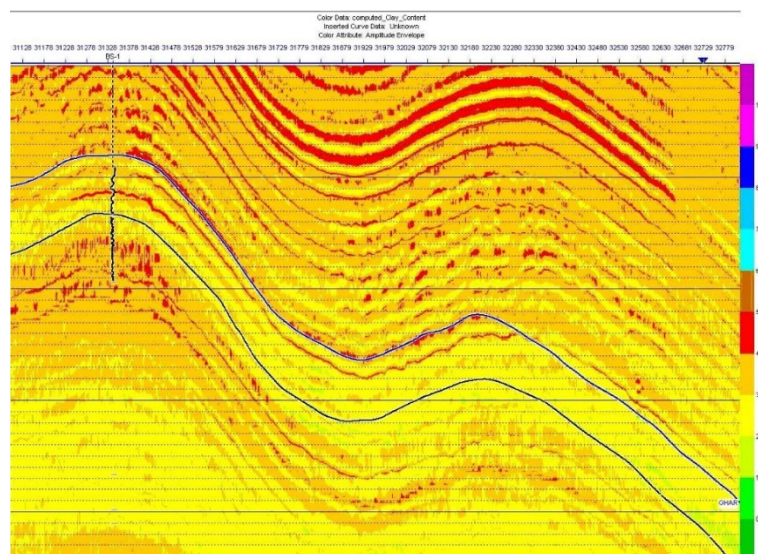


**Figure 24**

Shale volume was obtained across seismic line #7059 using PNN neural network method.

According to the results for shale volume (Figures 20-23), the amount of shale in the Hendijan hydrocarbon field is lower than that of the Bahregansar field. Both reservoirs are also divided into two upper and lower parts of the Ghar formation by a Shaly layer.



## Conclusion

We used seismic attributes that are sensitive to hydrocarbon petrophysical properties such as water saturation, porosity, and shale volume to study the Ghar formation. We estimated the reservoir porosity between 15% and 20% being higher in Hendijan than in the Bahregansar oilfield. The amount of the Ghar formation water saturation varies between 25 and 30 percent. On the other hand, the amount of clay content and shale volume in the Ghar formation in the Hendijan oilfield is higher than that of the Bahregansar oilfield. Based on the obtained results, the Ghar Formation was divided into two parts: a shaly layer which is the upper part of the formation and is more saturated than the lower part. We conclude that the Ghar formation horizon in the Hendijan oilfield has better hydrocarbon quality than the Bahregansar.

## Acknowledgments

This research did not receive any specific grant from funding agencies in the public, commercial, or not-for-profit sectors.

## References

- Abdel-Fattah, M. I., Pigott, J. D., and El-Sadek, M. S., Integrated Seismic Attributes and Stochastic Inversion for Reservoir Characterization: Insights from Wadi Field (NE Abu-Gharadig Basin, Egypt), *Journal of African Earth Sciences*, Vol. 161, 103661 P., 2020.
- Abdulaziz, A. M., The Effective Seismic Attributes in Porosity Prediction for Different Rock Types: Some Implications from Four Case Studies, *Egyptian Journal of Petroleum*, Vol. 29, No. 1, p. 95-104, <https://doi.org/10.1016/J.Ejpe.2019.12.001>, 2020.
- Abdulaziz, A.M., Mahdi, H.A., and Sayyauh, M.H., Prediction of Reservoir Quality Using Well Logs and Seismic Attributes Analysis with An Artificial Neural Network: A Case Study from Farrud Reservoir, Al-Ghani Field, Libya. *J. Appl. Geophys.*, No.161, p. 239-254, 2019.
- Abdulaziz, A. M., Mahdi, H. A., and Sayyauh, M. H., Prediction of Reservoir Quality Using Well Logs and Seismic Attributes Analysis with An Artificial Neural Network: A Case Study from Farrud Reservoir, Al-Ghani Field, Libya. *Journal of Applied Geophysics*, Vol. 161, p. 239-254, 2019.
- Alsharhan, A. E., Nairn, M., A Review of The Cretaceous Formations in The Arabian Peninsula and Gulf: Part I, Lower Cretaceous (Thamama Group), *Stratigraphy and Paleogeograph*, *Journal of Petroleum Geology*, Vol. 9, p. 365-392, 1986.
- Berthold, M.R., Diamond, J., Constructive Training of Probabilistic Neural Networks, *Neurocomputing*, Vol. 19, p. 167–183, 1998.
- Brown, A., Understanding Seismic Attributes, *Geophysics*, Vol. 66, No. 1, p. 47-49, 2001.
- Faraji, M. A., Kadkhodaie, A., Rezaee, R., and Wood, D. A. Integration of Core Data, Well Logs, and Seismic Attributes for Identification of The Low Reservoir Quality Units with Unswept Gas in The Carbonate Rocks of The World's Largest Gas Field, *Journal of Earth Science*, Vol. 28, No. 5, p. 857-866, 2017.
- Hampson, D.P., Schuelke, J.S., and Quirein, J.A., Use of Multi Attributes Transform to Predict Log Properties from Seismic Data. *Geophysics*, Vol. 66, p. 230-236, 2001.
- Hollis, C., Diagenetic Controls on Reservoir Properties of Carbonate Successions Within the Albian–Turonian of The Arabian Plate, *Petroleum Geoscience*, Vol. 17, No. 3, p. 223-241, 2011.

- Kadkhodaie-Ilkhchi, A., Rezaee, M.R., Rahimpour-Bonab, H., Chehrazi, A. Petrophysical Data Prediction from Seismic Attributes Using Committee Fuzzy Inference System, *Computers & Geosciences*, Vol. 35, No. 12, p. 2314-2330, <https://doi.org/10.1016/j.cageo.2009.04.010>, 2009.
- Mao, K.Z., Tan, K.-C., Ser, W., Probabilistic Neural-Network Structure Determination for Pattern Classification, *IEEE Trans, Neural Networks*, Vol.11, p. 1009–1016, 2000.
- Mohebbali, B., Tahmassebi, A., Meyer-Baese, A., Gandomi, A.H. Handbook of Probabilistic Models, p. 347–367, <https://doi.org/10.1016/B978-0-12-816514-0.00014-X>, 2020.
- Lang, X., & Grana, D., Geostatistical Inversion of Prestack Seismic Data for The Joint Estimation of Facies and Impedances Using Stochastic Sampling from Gaussian Mixture Posterior Distributions. *Geophysics*, Vol. 82, No. 4, p. 55-65, 2017.
- Lapponi, G., Casini, I., Sharp, W., Blendinger, N. Fernandez, I., Romaine, D. Hunt, “From Outcrop to 3D Modelling: A Case Study of a Dolomitized Carbonate Reservoir, Zagros Mountains, Iran”, *Petroleumgeoscience*, Vol. 17, p. 283-307, 2011.
- Maurya, S. P., Singh, K. H., Kumar, A., & Singh, N. P., Reservoir Characterization Using Post-Stack Seismic Inversion Techniques based on Real Coded Genetic Algorithm, *Jour. of Geophysics*, Vol.39, No. 2, 2018.
- Rastegarnia, M., Kadkhodaie, A., Estimation of Flow Zone Indicator Distribution by Using Seismic Data: A Case Study from A Central Iranian Oilfield, *Iranian Journal of Oil & Gas Science and Technology*, Vol. 2, No. 4, p. 12-25, 2013.
- Russell, B.H., The Application of Multivariate Statistics and Neural Networks to The Prediction of Reservoir Parameters Using Seismic Attributes. Ph.D., Dissertation, University of Calgary, Department of Geology and Geophysics, 2004.
- Russell, B.H., and Hampson, D., The Old and The New in Seismic Inversion, *CSEG Recorder*, Vol. 31, No. 10, p. 5-11, 2006.
- Russell, B.H., Introduction to Seismic Inversion Methods, Course Notes Series, No. 2, Society of Exploration Geophysicists, 90 P., 1988.
- Setudenhia, A., The Mesozoic Sequence in Southwest Iran and Adjacent Area, *Journal of Petroleum Geology*, Vol.1, No.1, p. 3–42, 1978.
- Sharland P. R., Archer R., Casey D. M., Davis R. B., Hall S. H., Heward A. P., Horbury A. D., and Simmons M. D., Arabian Plate Sequence Stratigraphy, *Geoarabia Special Pub.*, Gulf Petro Link, Bahrain., 371 P., 2001.
- Sheriff, R. E., *Encyclopedic Dictionary of Applied Geophysics*, SEG, 2002.
- Sharifi, J., Sabeti, N., Saberi, M.R., Sokouti Diarjan, M.R., Identify and Correction of The Borehole Effect on Petrophysical Logs, 17<sup>th</sup> Iranian Geophysical Conference, Tehran, Iranian Geophysical Association. (in Persian), 2016.
- Shiri, S., and Falahat, R., Rock Physics Modeling and 4D Seismic Feasibility Study in One of The Iranian Carbonate Reservoirs, *Journal of Applied Geophysics*, 103855, 2019.
- Taner, M. T., Schuelke J. S., O’Doherty R., and Baysal E., *Seismic Attributes Revisited 64<sup>th</sup> SEG Annu. Int., Meeting Vol. 13*, 1104 P. (Expanded Abstracts), 1994.
- White, R.E., Properties of Instantaneous Seismic Attributes, *The Leading Edge*, Vol. 10, No. 7, p. 26-32, 1991.

Xu, Z., Hu, S., Wang, L., Zhao, W., Cao, Z., Wang, R., ... & Jiang, L., Seismic Sedimentologic Study of Facies and Reservoir in Middle Triassic Karamay Formation of The Mahu Sag, Junggar Basin, China. *Marine and Petroleum Geology*, Vol. 107, p. 222-236, 2019.

Ziegler, M.A., Late Permian to Holocene Paleofacies Evolution of The Arabian Plate and Its Hydrocarbon Occurrences., *Georabia*, Vol. 6, p. 445-504, 2001.



#### COPYRIGHTS

©2023 by the authors. Licensee Iranian Journal of Oil & Gas Science and Technology. This article is an open access article distributed under the terms and conditions of the Creative Commons Attribution 4.0 International (CC BY 4.0) (<https://creativecommons.org/licenses/by/4.0/>)